Analytic models for a rapidly spinning spherical satellite charging in sunlight

Maurice Tautz
AER/Radex Inc., Lexington, Massachusetts, USA

Shu T. Lai
Space Vehicles Directorate, Air Force Research Laboratory, Hanscom Air Force Base, Massachusetts, USA

Received 14 September 2004; revised 24 March 2005; accepted 7 April 2005; published 19 July 2005.

[1] We present elementary analytic models for a fast-spinning, dielectric-coated, spherical spacecraft charging in sunlight. The models are based on a multipole expansion of Laplacian potentials external to the spacecraft surface. We assume azimuthal symmetry about the spin axis, and the spin period must be short compared with surface differential charging times. There are three parameters in the models: the monopole potential, the relative strength of the dipole/quadrupole components with respect to the monopole, and a mixing angle. The combination of monopole potentials along with the dipole or quadrupole contributions produce potential barriers which form at the satellite surface. These barriers can act to block escaping photoelectrons and lead to current balance, allowing sunlight charging to high negative levels. The sunlit side charges less (negatively) than the shade side and the ratio of Sun to shade potentials is near its threshold value for high-level charging. We have calculated more general cases with various values of Sun angle relative to the spin axis by combining the dipole and quadrupole components. The potential barrier shape and area vary for different cases and the maximum barrier approximately follows the Sun angle. We stress that for physical interpretation of data obtained on board, one should take into account the potential distribution and where the instrument is located.

Citation: Tautz, M., and S. T. Lai (2005), Analytic models for a rapidly spinning spherical satellite charging in sunlight, *J. Geophys. Res.*, *110*, A07220, doi:10.1029/2004JA010787.

1. Introduction

[2] Spacecraft charging occurs when there is build up of charge on exposed external surfaces of a satellite due to interaction with the ambient space environment. There are two main types of charging: absolute charging, which occurs when the entire spacecraft potential relative to the space plasma is changed, and differential charging, where parts of the spacecraft go to different potentials relative to each other. The result can be degradation of surface properties and disruption of spacecraft operations. The spacecraft charging phenomena is a key issue of space physics, since it is both a consequence of the space environment and an important consideration for space plasma characterization from a charged satellite. We develop here simple analytic models of daylight differential charging which enable one to capture the first-order features of the charging of fast spinning satellites in sunlight.

[3] It is known that a satellite in sunlight can charge to substantial negative voltages, even though the photoelectron current (positive) is typically much larger than the ambient currents in space. This effect occurs because photoelectrons escaping from the satellite surface can be blocked by local potential barriers. The formation of such a barrier is a multidimensional effect, where shaded surfaces build up to high negative potentials and then wrap around to suppress the escape of low-energy electrons elsewhere on the satellite. When the outgoing flux of photoelectrons is reduced in this way, current balance on the satellite can be readily achieved. In this paper, we consider charging models which are based on blocked photoelectron currents.

[4] For a real spacecraft with various surface elements, there will be approximate azimuthal symmetry if the satellite is rapidly rotating so that it experiences only time-averaged photoemission. By rapid motion, we mean that the differential charging time is long compared with the spin period. Many space research satellites at geosynchronous altitudes feature rapid spinning and dielectric surfaces. For example, the spacecraft potential of the Los Alamos National Laboratory (LANL) geosynchronous satellites is determined based on the spin-averaged energy spectra for ions and electrons (M.F. Thomsen, personal communication, 2002).

[5] The existence of potential barriers, though never explicitly measured, has been inferred from the electron energy spectra observed at a spot on the surface on the ATS-5 satellite [*Olsen*, 1980; *Olsen et al.*, 1981] and on ISEE 1 [*Olsen and Whipple*, 1988] previously. Potential barriers

0148-0227/05/2004JA010787$09.00

were also of concern for the Geotail and Cluster satellites [*Zhao et al.*, 1996; *Thiebault et al.*, 2004]. We remark that the distribution of the satellite surface potential has not been measured on the LANL satellite or any other spacecraft. For example, the SCATHA [*Stevens and Vampola*, 1978] satellite potential was measured on the ends of two booms [*Lai*, 1994], on four very small pieces of adjacent surfaces, and by means of the ion spectrum measured at a spot. Such spotty measurements were insufficient to map the potential distribution. At the present, there is no in-flight measurement available for comparison with models of satellite potential distributions. Such measurements can be done on future satellites if properly equipped.

[6] There are benefits for modeling potential distributions. For example, in considering current balance in sunlight, one needs to know how much of the photoelectron current emitted from the spacecraft surfaces is blocked by potential barriers. Current balance determines the equilibrium potential of spacecraft surfaces. Since photoelectrons are of low energy (temperature $\approx$1.2 eV), they are sensitive to potential barriers. In general, the potential height, shape, and spatial distribution of barriers are important factors affecting the escape of photoelectrons. If these factors are known, one can even calculate the trajectories of the photoelectrons reflecting back from, or escaping through, the barriers. If most of the photoelectron current escapes, it would mostly likely exceed the ambient current and control the charging of the surfaces. For geophysical applications, the researchers often need to estimate the effect of charging on the instruments which are located on, or are protruding from, satellite surfaces. The models feature a potential barrier in the region receiving sunlight at or near normal incident angle. The effects on the instrument can be very different depending on where the instruments are in the potential distribution. Therefore there is a need to better model and understand simple potential distributions on spacecraft.

[7] The analytic models that are considered assume azimuthal symmetry around the spin axis and Laplacian potentials. The potentials exterior to a spherical satellite with azimuthal symmetry can be expanded in a series of multipole terms. Here we keep the three lowest-order terms: the monopole, dipole, and the quadrupole. There are two special combinations of interest: the monopole-dipole model and the monopole-quadrupole model. The monopole-dipole model, where the satellite is nonrotating, has been treated by *Besse and Rubin* [1980], *Mandell et al.* [1978], and *Higgins* [1979]. The monopole-quadrupole model has been treated by *Tautz* [2003]. In the monopole-dipole model we can interpret the Sun as shining on a spin axis pole, and in the monopole-quadrupole model the Sun is shining at the belly band of the satellite. In this paper, we discuss the above models in relation to the more general case, where the Sun direction angle with respect to the spin axis is arbitrary.

[8] The formation of a potential barrier is the main driver for daylight charging, since it can block escaping photoelectrons and allow negative charging even on sunlit surfaces. Analytic models, although giving only a simplified representation of reality, are relevant to spacecraft charging because they help understand the physics, provide first estimates, and describe limit cases. The analytic monopole-dipole-quadrupole models given here are based on barriers that form from linear combinations of azimuthally symmetric Laplacian potentials. The resulting field surrounding the spacecraft represents the approximate shape of the charging response in daylight of a fast-spinning, roughly spherical, mostly nonconducting satellite in a low-density space plasma environment. Any satellite in these conditions would approach the models.

[9] There are three parameters in the analytic models. The first parameter, K, is the monopole potential. The second parameter, A, is the dipole/quadrupole strength relative to the monopole. The third parameter, θ, is the mixing angle. The basic equations of the models and their parameters are described in section 2. In section 3, numerical solutions are outlined and results are given in (A, θ) space. The solutions are depicted by color contour plots of the potentials in the physical space surrounding the satellite for several mixing angles. In section 4, we discuss real sunlight charging in space and make a brief reference to experimental results. Section 5 contains summary remarks.

2. Description of the Models

[10] For a dielectric covered satellite rotating in sunlight, the characteristic time for differential charging of a surface area element can be estimated from the equation $J\Delta t = C\Delta V$, where C is the capacitance per unit area, ΔV is the charging voltage, and J is the driving photoelectron current density. The value of C depends on the surface material properties: $C \sim \epsilon\epsilon_o/d$, where ϵ is the relative dielectric constant and d is the thickness. Given ϵ = 2.0 (Teflon) and a thickness of 10^{-4} m, we get C = 0.2 μf.m^{-2}. If we put in some typical values (ΔV = 3 kV, $J = 10^{-5}$ A m^{-2}), we find $\Delta t \sim$ 60 s. This number could vary by an order of magnitude, depending on the surface conditions. If the spin period is much longer than Δt (slow motion), the surface can react in time to follow the Sun. If the spin period is short compared with Δt (rapid motion), the surface has time to react only to a rotation averaged solar illumination.

[11] Plasma potentials are obtained from Poisson's equation, which in dimensionless form is $\nabla^2\chi = \rho/\lambda^2$, where $\chi = e\phi/kT$, T is temperature, ρ is the sum of the normalized ion and electron densities, and λ is the Debye length. If λ is a few meters to kilometers in length, as is often the case in geosynchronous orbits, the ambient density term may be neglected and Laplace's vacuum equation used. Even when solving Poisson's equation in the photoelectron barrier region, the space charge has only a small effect for high-voltage differential charging (as indicated by *Mandell et al.* [1978]) and may be omitted. We use Laplacian potentials throughout this paper.

[12] Consider a dielectric covered spherical satellite that is spinning rapidly in sunlight so that only time-averaged rotational effects are important. For this case, there is approximate azimuthal symmetry around the spin axis. If the ambient charge density is low, which often occurs at geosynchronous altitudes, the potentials outside such a satellite are given approximately by a solution to Laplace's equation. In spherical coordinates, the azimuthally symmetric exterior Laplacian potentials are of the form (see *Schwartz* [1972]):

$$V(r,t) = \sum_{n=0}^{\infty} B_n \frac{P_n(t)}{r^{n+1}}, \tag{1}$$

where r is the radius and t is the angle from the north pole. The sum is over $n = 0, 1, 2\ldots$ and $P_n(t)$ is the nth-order Legendre polynomial. The constant coefficients B_n depend on the exterior conditions. For convenience, we can factor out the first term so that

$$V(r,t) = \frac{K}{r}\sum_{n=0}^{\infty}\frac{A_n P_n(t)}{r^n}, \tag{2}$$

where $K = B_0$ is the monopole potential and the coefficients $A_n = B_n/K$ give the strength relative to the monopole. In this paper we consider the first three terms in the expansion, i.e., $A_0(=1)$, A_1, A_2 and their corresponding Legendre polynomials:

$$P_0(t) = 1, \qquad P_1(t) = \cos(t), \qquad P_2(t) = \frac{3\cos^2(t) - 1}{2}. \tag{3}$$

There are two cases of special interest:

$A_1 = -A$, $A_2 = 0$: the monopole-dipole solution.
$A_1 = 0$, $A_2 = A$: the monopole-quadrupole solution.

Note that the minus sign in the monopole-dipole case is arbitrary: it puts the Sun direction at the north spin pole instead of the south. In the monopole-quadrupole case, the Sun is considered to be at the belly band [*Tautz*, 2003].

[13] The K parameter in the models depends on the balance of the incoming and outgoing satellite surface currents and for negative charging is less than zero. The A parameter, which gives the strength of the nonmonopole contribution to the expansion, is also set by current balance. Thus in sunlight a potential barrier forms just outside the sphere surface, which, for a certain A value, suppresses escaping photoelectrons so that a balance can be made with the other currents to the satellite. Since the currents are here not assumed to be known, K and A are free parameters of the models.

[14] We now wish to consider the more general case where the Sun angle lies somewhere between the directions given in the above two models. To this end, we introduce the parameterization

$$A_1 = -A\cos\theta \tag{4}$$

$$A_2 = A\sin\theta, \tag{5}$$

where θ is a mixing angle measured with respect to the spin axis. The minus sign is again arbitrary and agrees with previous treatments. This parameterization allows for a continuous Sun modulation of the solutions and is chosen so that we recover the special cases

$\theta = 0^\circ$ $\rightarrow$ the monopole-dipole solution (Sun at north pole)
$\theta = 90^\circ$ $\rightarrow$ the monopole-quadrupole solution (Sun at belly-band)
$\theta = 180^\circ$ $\rightarrow$ the reversed monopole-dipole solution (Sun at south pole).

Using the above A, θ parameterization, the expression for V becomes

$$V(r,t) = \frac{K}{r}\left[1 + A\left(\frac{-\cos\theta P_1(t)}{r} + \frac{\sin\theta P_2(t)}{r^2}\right)\right]. \tag{6}$$

Since the above potentials scale with K, we can analyze the problem mainly in terms of A and θ and employ the normalized potentials $V(r, t)/K$.

[15] Using the reflection symmetries of the Legendre polynomials ($P_1(180^\circ - t) = -P_1(t)$ and $P_2(180^\circ - t) = P_2(t)$), we find

$$V(r, 180^\circ - t) = \frac{K}{r}\left[1 + A\left(\frac{\cos\theta P_1(t)}{r} + \frac{\sin\theta P_2(t)}{r^2}\right)\right], \tag{7}$$

which differs from $V(r, t)$ only by the sign in the cosine term. If we make the further parameter transformation $\theta \rightarrow 180^\circ - \theta$, we get back $V(r, t)$. This shows that models related by the θ transformation have reflection symmetry about the belly band. Since the angle $\theta = 0^\circ$ maps into 180°, the monopole-dipole and reversed monopole-dipole models are essentially the same, except that the north and south poles are switched.

[16] If we assume a unit radius sphere, we have on the surface

$$V(1,t) = K[1 + A(-\cos\theta P_1(t) + \sin\theta P_2(t))] \tag{8}$$

and we get by substitution the north, middle, and south surface potentials

$$\begin{aligned} V(1,0) &= V_N = K(1 + A(-\cos\theta + \sin\theta)) \\ V(1,90^\circ) &= V_M = K(1 - A(\sin\theta)/2) \\ V(1,180^\circ) &= V_S = K(1 + A(\cos\theta + \sin\theta)) \end{aligned} \tag{9}$$

For the axis aligned with the Sun ($\theta = 0^\circ, 180^\circ$), the sine is zero and we have $V_M = K$. For the Sun direction orthogonal to the spin axis ($\theta = 90^\circ$), the cosine is zero and we have $V_S = V_N$. Other values of the surface potentials for the monopole-dipole and monopole-quadrupole special cases are summarized in Appendix A. Under the θ transformation, $V_S \rightarrow V_N$, $V_N \rightarrow V_S$, and $V_M \rightarrow V_M$. The above relations can be inverted to yield back K, A, and θ:

$$K = (V_N + V_S + 4V_M)/6 \tag{9'}$$

$$A = \left(1 - \frac{V_N + V_S}{K} + \frac{V_N^2 + V_S^2}{2K^2}\right)^{1/2} \tag{10}$$

$$\theta = \cos^{-1}\left(\frac{V_S - V_N}{2KA}\right). \tag{11}$$

Thus the three measured potentials V_S, V_M, and V_N could be used to estimate the model parameters K, A, and θ. Two surface potential ratios of physical interest are (north-to-south):

$$\frac{V_N}{V_S} = \frac{1 + A(\sin\theta - \cos\theta)}{1 + A(\sin\theta + \cos\theta)}. \tag{12}$$

and (middle-to-south):

$$\frac{V_M}{V_S} = \frac{1 - (A\sin\theta)/2}{1 + A(\sin\theta + \cos\theta)}. \tag{13}$$

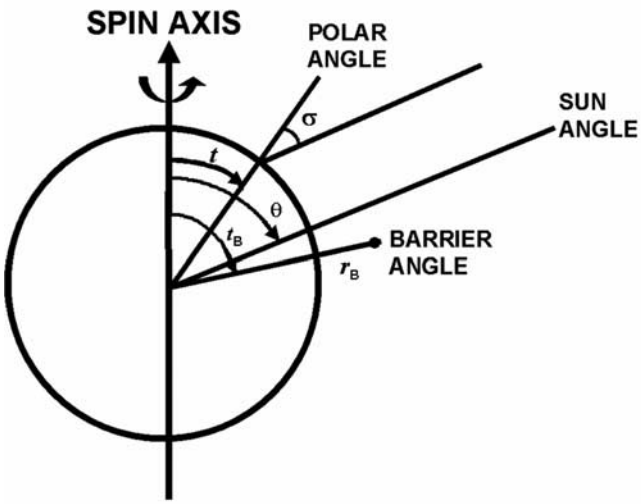

Figure 1. Angles in the sunlight charging models. One recovers the monopole-dipole model if θ = 0° and the monopole-quadrupole model if θ = 90°.

These ratios compare approximate shade and sunlit side charging levels and are independent of K.

3. Numerical Solution of the Models

[17] For substantial negative charging to occur in sunlight, we expect a potential barrier to form just outside the surface, in order to trap escaping photoelectrons. Such a barrier exists if

$$dV(r,t)/dr = 0 \tag{14}$$

has a solution. Using the previous expression for $V(r, t)$, we get

$$\frac{K}{r^2}\left(1 - \frac{2\cos\theta A P_1(t)}{r} + \frac{3\sin\theta A P_2(t)}{r^2}\right) = 0, \tag{15}$$

which gives a quadratic equation for r:

$$r^2 - 2\cos\theta A P_1(t) r + 3\sin\theta A P_2(t) = 0. \tag{16}$$

The solution r_b for the barrier radius is thus

$$r_b(A,\theta,t) = \cos\theta A P_1(t) + \left[(\cos\theta A P_1(t))^2 - 3\sin\theta A P_2(t)\right]^{1/2}. \tag{17}$$

Since r_b is a function of the angle t, we can find the value of $t = t_B(A, \theta)$ that makes the barrier radius a maximum, r_B, and which can be used to define the barrier angle. At such a t value, if $r_B > 1.0$, then the potential barrier lies outside the surface. The angles in the problem are shown in Figure 1.

[18] A barrier forms only for certain values above a threshold depending on A and θ. The value of the threshold can be determined from the condition $r_B = 1.0$. Here we have obtained r_B at each A and θ by solving numerically the equation

$$r_B = r_b(A,\theta,t_B(A,\theta)). \tag{18}$$

In the analysis, t_B was initially found by sweeping through the range of t and saving the angle giving the maximum r_B. Subsequently, this method was augmented by an analytic calculation (see Appendix B). We note that t_B is not always aligned with the mixing angle θ direction. This alignment is true for the poles and at the belly band but not for the between angles. The angle t_B can be thought of as a crude indicator of the Sun direction. Since there is an approximate correspondence between t_B and θ, we can interpret the mixing angle θ as roughly pointing toward the Sun.

[19] In Figure 2 we have plotted the r_B results in (A, θ) space. The contour line with $r_B = 1.0$ represents the threshold boundary for barrier formation. Points to the right of this line can charge. One can see that there is structure to the thresholds. A minimum threshold A value occurs with the Sun at the spin poles (θ = 0°, 180°) and a lesser minimum at the belly band (θ = 90°), while maxima are found at about θ = 25 and 155 degrees.

[20] The height of the potential barrier was taken as

$$V_B = V(r_B, t_B) - V(1, t_B), \tag{19}$$

and a plot of V_B in (A, θ) space is given in Figure 3. Since the potential is proportional to K, it is convenient to plot the normalized quantity V_B/K. Note that at the threshold, $V_B = 0$ and hence this contour line follows the r_B threshold line given in Figure 2.

[21] In order to get a representation of the Sun to shade charging ratio, we introduce a variable:

$$V_{SS} = V_{\text{sun}}/V_{\text{shade}}, \tag{20}$$

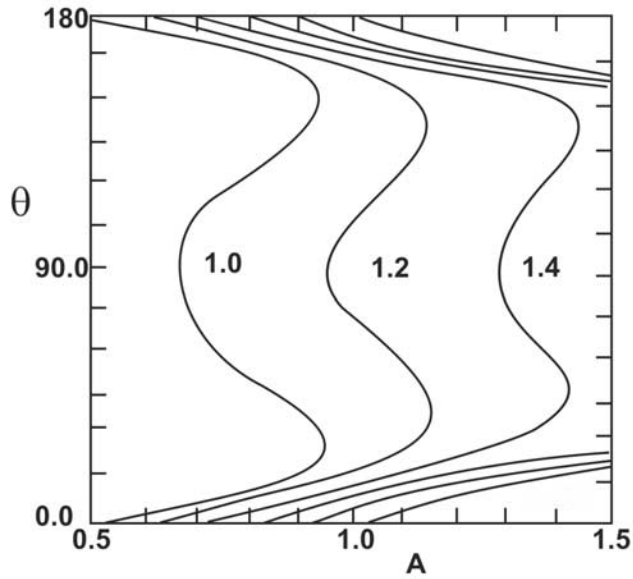

Figure 2. The radius r_B of the maximum potential barrier versus A and theta. The value of r_B is in units of the satellite radius. Here θ = 0° corresponds to the spin axis being parallel to sunlight, while θ = 90° corresponds to sunlight shining on the belly band. At θ = 0°, r_B starts at unity when the A reaches the threshold value of 0.5. At θ = 90°, r_B starts at unity when A reaches the threshold at 0.667.

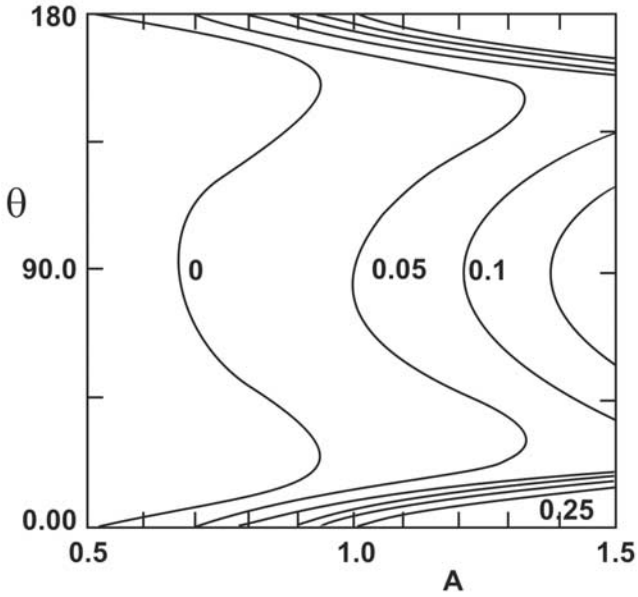

Figure 3. Barrier potential V_B/K versus A and θ. At θ = 0°, the barrier potential starts at zero when the A reaches the threshold value of 0.5. At θ = 90°, the barrier potential starts at zero when A reaches the threshold at 0.667.

where normalized V_{shade} gives the largest charging level away from the Sun

$$V_{\text{shade}} = \text{Max}(\, V_S/K,\ V_N/K\,) \tag{21}$$

and normalized V_{sun} gives the charging level underneath the potential barrier

$$V_{sun} = V(1, t_B)/K. \tag{22}$$

The V_{SS} ratio allows for a smooth transformation from V_N/V_S at θ = 0° to V_M/V_S at θ = 90° and to V_S/V_N at θ = 180°. A plot of V_{SS} is given in Figure 4. It can be seen that the ratio is 0.33 at the spin pole thresholds and 0.4 at the belly band. The symmetry about θ = 90° is evident.

[22] Figures 5a–5f show the model solutions for various mixing angles in the physical space surrounding the sphere. The contour plots show a $Y = 0$ slice of data expressed in X, Y, Z coordinates, which are normalized to the sphere radius. All potentials have been normalized to K. The A parameter has been selected so that the barrier potential ratio $V_B/K \sim 0.01$. This sets up a barrier of −10 V, given a monopole potential of −1000 V. The plots are given for six angles θ = 0, 30, 45, 60, 90, and 180 degrees. In the figures, the mixing angle is denoted by a radial white line. One can see that an azimuthally symmetric potential barrier approximately follows the θ angle as it goes from the north spin pole to the south. Figures 5a, 5e, and 5f show the monopole-dipole, monopole-quadrupole, and reversed monopole-dipole systems. The pair of Figures 5a and 5f illustrate the model reflection symmetry with respect to the belly band, for systems related by the mixing angles θ and 180° − θ.

4. Real Sunlight Charging

[23] Photoemission currents (positive) usually dominate over other ambient currents in the magnetosphere. Therefore by using straightforward current balance, we might expect charging to positive levels. Yet negative spacecraft charging is reported not only in eclipse but also sometimes in sunlight. A bootstrap mechanism for sunlight charging is known. The shaded surfaces charge up and the fields wrap around the satellite and set up a potential barrier over the sunlit surfaces. Photoelectrons emitted from the sunlit surfaces encounter the radial barriers and a fraction is returned. The barrier height adjusts until the total net current to the satellite goes to zero.

[24] In this paper we keep only the first three terms in the potential expansion so that the treatment is approximate, even in the simple cases of mixing (θ = 0°, 90°). It is impossible within this framework to give a self-consistent treatment of the photoemission dynamics. To do this would require solving Poisson's equation using the electron space charge density and tracking the photoelectrons to determine the net current. In order to trap the outgoing electrons, an area with significant photoemission must have a potential barrier on top of it. A real satellite would be exposed to 180 degrees of sunlight, whereas the barrier regions in our simplified models can be much smaller than this. This situation cannot be self-consistent because all photoelectrons outside of this region would escape, giving a reduced potential. On the other hand, the solar flux projected on a spherical surface decreases by the cosine of the angle of incidence and the photoemission yield will also go down with angle of incidence due to reflection at the surface so that the effective area of exposure is reduced from 180 degrees (see below). Also, in the models, the width and height of the barrier tend to grow larger as the A parameter is increased from threshold, leading to more trapped photoelectrons. The above remarks are in the right direction, but we cannot expect that the real potential

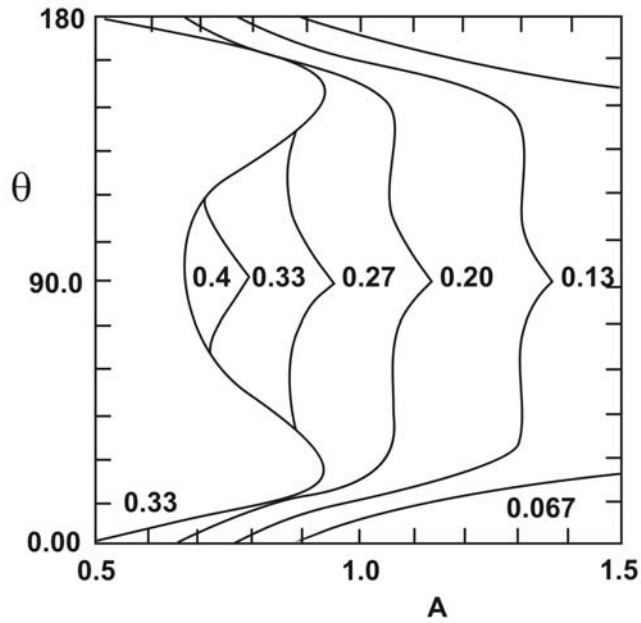

Figure 4. Sun to shade potential ratio V_{SS} versus A and theta. At θ = 0°, the ratio equals about 0.33 when A equals 0.5, the threshold value. At θ = 90°, the ratio equals 0.4 when A reaches the threshold at 0.667. The first line gives values along the threshold boundary curve seen in Figures 2 and 3.

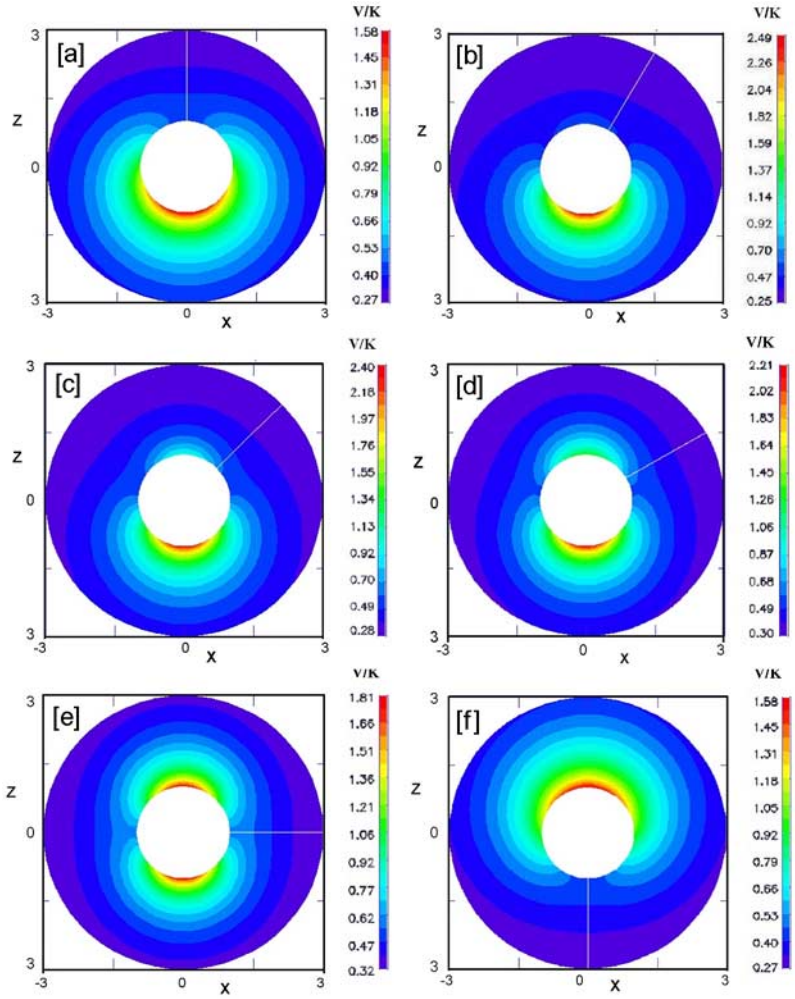

Figure 5. (a) Normalized potentials for the case $\theta = 0°$, $V_B/K = 0.01$. $Y = 0$. This is a monopole-dipole case. The spin axis is vertical and parallel to the sunlight direction. High negative potentials appear on the shadowed side. (b) Normalized potentials for the case $\theta = 30°$, $V_B/K = 0.01$. $Y = 0$. The spin axis is vertical. The sunlight direction is along the 30° line. (c) Normalized potentials for the case $\theta = 45°$, $V_B/K = 0.01$, $Y = 0$. The spin axis is vertical. The sunlight direction is along the 45° line. (d) Normalized potentials for the case $\theta = 60°$, $V_B/K = 0.01$. $Y = 0$. The spin axis is vertical and the sunlight direction is along the 60° line. Note the symmetry about the spin axis but not with respect to the sun direction. (e) Normalized potentials for the case $\theta = 90°$, $V_B/K = 0.01$. $Y = 0$. This is the monopole-quadrupole case. The spin axis is vertical and perpendicular to the sunlight direction. The symmetry with respect to the sunlight direction is apparent. (f) Normalized potentials for the case $\theta = 180°$, $V_B/K = 0.01$. $Y = 0$. This is a reverse monopole-dipole case similar to that in Figure 5a but with the spin and the sunlight direction antiparallel to each other.

profile, self-consistent with photoemission dynamics, to be obtained by our approximate models.

[25] Laboratory measurements show that photoelectrons are approximately Maxwellian with a few eV in energy [*Hinteregger et al.*, 1959; *Feurenbacher and Fitton*, 1972; *Wrenn and Heikkila*, 1973; *Whipple*, 1981]. The fraction f of photoelectron flux escaping a linear barrier of height $B > 0$ scales as

$$f \propto \exp(-B/T_{ph}), \tag{23}$$

where T_{ph} is the photoelectron temperature. In order to significantly reduce the outgoing photoemission current, B needs to be a few times T_{ph}, but since T_{ph} at geosynchronous altitudes is typically small (~1.2 eV) [*Whipple*, 1981; *Lai et al.*, 1986], B would need to be only of order 10 V to suppress most of the photoemission flux emerging below the barrier.

[26] Photoemission can occur on surfaces instantaneously exposed to sunlight. For a spinning satellite the shaded areas could be characterized by $\sigma = t - \theta >= 90°$, where σ is the Sun angle of incidence (see Figure 1). This is because on a sphere, area element normals have a $\cos(\sigma)$ projection in the light direction. For example, in the monopole-quadrupole case, where the Sun is at the belly band, this criterion strictly includes just the north and south spin poles. However, there is another important effect to consider, the surface reflectance increases with the incident angle. As

an effect of this property, the photoemission per unit area further diminishes. The photoelectron current as a function of the reflectance R [see, e.g., *Samson*, 1967] is given by

$$I_{ph}(R) = I_{ph}(0)[1 - R(\sigma, \omega)], \tag{24}$$

where ω is the light frequency. The reflectance $R(\sigma)$ is a minimum at normal incidence and maximum to unity at grazing incidence ($\sigma = 90°$) (for typical graphs, see *Powell* [1970] and *Lai et al.* [1986]). The photoemission currents are thus expected to decrease with incident angle by the factor

$$g = \cos(\sigma)\left[\frac{1 - R(\sigma, \omega)}{1 - R(0, \omega)}\right], \tag{25}$$

and hence there is a corresponding increase in the effective shaded area.

[27] The emerging low-energy photoelectrons are steered toward the barrier region by the local fields. In high-level charging, the barrier potential $B = -V_B$ from the models is small compared with other potentials in the problem (K can be in the kV range), and the model tends to be near the threshold limit at $V_B/K = 0.0$. This can be seen by looking at Figures 2 and 3. The Sun-to-shade potential ratio V_{SS} is a maximum at the threshold values, which can be seen in Figure 4. The threshold limits of V_{SS} are 0.33 in the monopole-dipole cases ($\theta = 0, 180°$), 0.4 for the monopole-quadrupole case ($\theta = 90°$), and intermediate Sun angles can have lower values.

[28] Thus if we know the approximate angle θ, we can estimate the Sun-to-shade charging ratio from the model. The ratio will be less than or equal to the threshold. If the satellite is covered mainly by dielectrics, and there is minimal current transport between shade and Sun sides, this ratio corresponds approximately to measured sunlight to eclipse charging ratios. As a footnote, we emphasize again that the spacecraft surfaces are assumed to be insulating or not connected because uniform charging without barriers in sunlight would not enable high-level negative-voltage charging in sunlight to occur. Sunlight to eclipse charging ratios of 0.33 approximately have been observed (S. T. Lai and M. Tautz, High-level spacecraft charging in eclipse at geosynchronous altitudes: A statistical study, submitted mansucript, 2005) in the Los Alamos National Laboratory (LANL) satellite data. The LANL satellites have geosynchronous orbits and their spin period is ~10 s [*Bame et al.*, 1993]. The data for over 10 flight years and from five different satellites was looked at. Statistical plots of charging potentials in eclipse and in sunlight were accumulated versus electron temperature and the ratios calculated (Figure 6). In this figure, we have plotted the spacecraft potential versus the ambient electron temperature. The potential was obtained by identifying the peak in the ion energy distribution as the spacecraft potential (negative voltage). The measurements were in discrete energy channels. The discreteness manifest as the quantized behavior of the spacecraft potential in Figure 6. The centroid of all the data on the same quantized level is shown as a triangle. The ambient electron temperature was obtained by means of the moments of the electron distribution function. There are two branches in Figure 6, corresponding to charging in eclipse (upper curve) and in sunlight. The sunlight curve is smooth because the LANL team, having noticed the approximate dependence of spacecraft potential on the electron temperature, interpolated the sunlit branch to form a smooth curve. For our purpose, the details of the treatments of ion peaks and temperature moments are unnecessary; the reader interested in details is referred to *Bame et al.* [1993] and *Thomsen et al.* [1999]. Because the LANL satellites point toward the Earth center, the Sun angle on entering eclipse is similar to that of the monopole-dipole configuration which has a threshold V_{SS} value of 0.33. This shows that the simple models presented here have relevance to real charging cases in the fast spin limit.

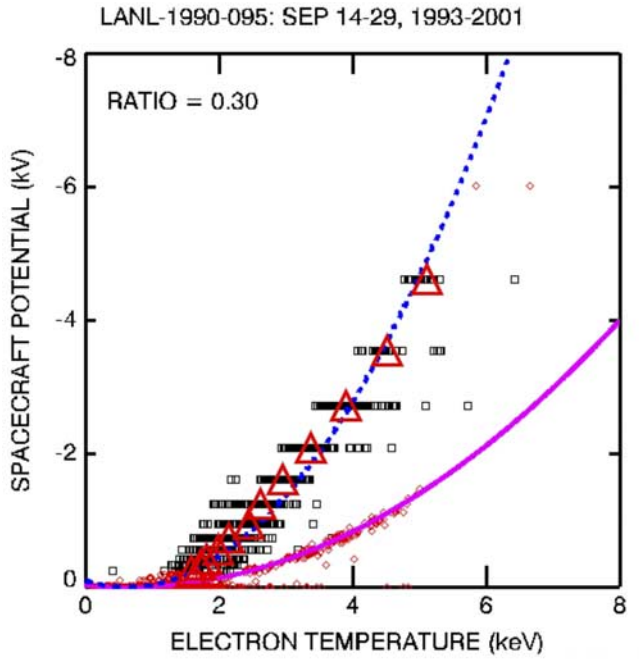

Figure 6. Plot of spacecraft potential versus ambient electron temperature obtained on Satellite LANL 1990-095, 13–19 September 1993–2001. The upper branch is for charging in eclipse and the lower branch in sunlight. Ratio of sunlight charging to eclipse charging is nearly 0.33. The spacecraft potential data appear quantized because of the way the instrument was designed. Each triangle represents the centroid of the data at the same quantized level. The sunlit data are not quantized because the LANL team has interpolated them to form a smooth curve.

[29] In a real physical charging case, the surface will not be exactly spherical and, indeed, if the surface is not smooth enough, the distance and shape of the barrier will be greatly affected by the surface geometry. In a real case, there also would not be exact azimuthal symmetry, although our approximation of symmetric potential tends to improve at higher spin rates. The surface materials of a real satellite may be quite varied and contain a mixture of dielectrics and conductors, with complicated electrical connections.

5. Summary and Conclusion

[30] When the ambient density is low, the potentials exterior to a spacecraft are given approximately by solutions

to the Laplace equation. A rapidly spinning satellite has approximate azimuthal symmetry around the spin axis, due to revolution time averaging. An azimuthally symmetric dielectric sphere will have a Laplace solution for the exterior potentials given in terms of a multipole expansion. The monopole-dipole combination represents a satellite with the spin axis pointed at the Sun and the monopole-quadrupole solution corresponds to a satellite with the Sun at right angles to the spin axis. In the general case, the Sun direction will make an arbitrary angle with respect to the spin axis and the potentials will be given by a combination of the above models.

[31] To build a model based on the general Sun orientation, the Laplace potential expansion coefficients were taken as a Sun direction modulation factor times an amplitude giving the relative strength of the dipole/quadrupole terms. For parameter values above threshold, the models will set up a potential barrier near to the Sun direction. The barrier height, which is a function of the model parameters, acts to suppress photoemission and ultimately to allow current balance on the satellite. The ratio of the sunlight-to-shade potentials on the satellite surface is predicted to be less than or equal to the threshold.

[32] The models will give a better representation of barrier-dominated daylight charging of spherical satellites as long as the following approximations are satisfied: there is azimuthal symmetry about the spin axes, the surface is covered uniformly with dielectric, and internal electrical connections may be ignored. The smoother the surfaces and the higher the spin rate, the better the approximation will be. The overall approximations are that ambient density is low enough that Laplace potentials may be used and that multipole terms higher than the quadrupole are not considered in the potential expansion. Self-consistent photoemission dynamics is not addressed by the models.

[33] For satellite applications, the distribution of potentials on a spacecraft affects the current flow of low-energy electrons, such as photoelectrons, to and from surfaces and onboard instruments. Besides differential charging affecting current balance, the interpretation of scientific data obtained on board often requires the knowledge of potential distribution and current flows in the vicinity of the intruments. As an example, an instrument located near the belly band in Figure 5a would experience different voltages and current flows from one in Figure 5e.

[34] As an improvement to previous models of potential distribution for geophysical applications, we stress that it is important to pay attention to the sunlight direction, the spin rate, and the capacitance charging time of the surfaces. We have studied the interesting case of high spin rate and long capacitance charging time. The models depend only on the monopole potential, K, the relative strength of the dipole/quarupole components, A, and the approximate Sun angle, θ.

[35] In the limit of spin axis being parallel to the sunlight direction ($\theta = 0°$), one recovers the monopole-dipole result: the ratio of potentials of the sunlit side and the shadowed side equals 0.33 at the charging threshold ($A = 0.5$). When the spin axis is perpendicular to the sunlight direction ($\theta = 90°$), the monopole-quadrupole system results: the ratio of the sunlit and shaded potentials equals 0.4 at the charging thresold ($A = 0.667$). Near the thresholds, the barrier height can be small compared with the monopole potentials, K, but is large enough to block emerging low-energy photoelectrons. We have calculated more general cases with various θ angles by combining the dipole and quadrupole terms. The barriers are azimuthally symmetric, but their shape and area vary for different θ angles and the location of the maximum barrier tends to follow θ. We stress that for physical interpretation of data obtained on board, one should take into account the potential distribution and where the instrument is located. We hope that the analytical formulation in this paper will be useful for guiding or helping the development of future numerical computational models of charging of rapidly spinning dielectric satellites in sunlight.

Appendix A: Special Case Parameters

[36] We collect here, for easy reference, parameters for the monople-dipole and the monopole-quadrupole models. The notation is the same as in sections 2 and 3.

[37] For the monopole-dipole model $\theta = 0°$:

$$V_N = K(1 - A)$$

$$V_M = K$$

$$V_S = K(1 + A)$$

$$V_{SS} = V_N/V_S.$$

The barrier radius is $r_b(t) = 2A\,P_1(t)$ with a maximum at $t = t_B = 0$, $r_B = 2A$.

At the charging threshold:

$$A = 1/2 : V_n = K/2,\ V_m = K,\ V_S = 3/2K.$$

For the monopole-quadrupole model $\theta = 90°$;

$$V_N = K(1 + A)$$

$$V_M = K(1 - A/2)$$

$$V_S = K(1 + A)$$

$$V_{SS} = V_M/V_S = V_M/V_N.$$

The barrier radius is $r_b(t) = \sqrt{(-3AP_2(t))}$ with a maximum at $t = t_B = 90°$, $r_B = \sqrt{(3/2\ A)}$.
At the charging threshold:

$$A = 2/3 : V_N = 5/3K,\ V_M = 2/3K,\ V_S = 5/3K$$

For the reversed monopole-dipole model $\theta = 180°$; replace A by $-A$ in the $\theta = 0°$ potential equations. The maximum radius is the same because $t_B = 180°$.

Appendix B: Calculating the Barrier Angle $t_B(A, \theta)$.

[38] To find the angle giving the maximum barrier radius,we use the condition

$$\frac{d\,r_b(A, \theta, t)}{dt} = 0, \tag{B1}$$

where $r_b(A, \theta, t)$ is given in section 3. This leads to the equation

$$\sin t\left[A_1 + 0.5\,(f(t))^{-1/2}\alpha\cos t\right] = 0, \tag{B2}$$

where we define

$$f(t) = (A_1 P_1(t))^2 - 3A_2 P_2(t) \tag{B3}$$

and

$$\alpha = -2A_1^2 + 9A_2. \tag{B4}$$

Here A_1, A_2 are the same as in section 2 and the $P_1(t)$, $P_2(t)$ are Legendre polynomials. We let $x = \cos t$ and solve the bracket part of equation (B2) for x, giving

$$x = \left[\frac{(6A_2\gamma^2)}{1 + 2\gamma^2\alpha}\right]^{1/2}, \tag{B5}$$

where we have further defined

$$\gamma = A_1/\alpha. \tag{B6}$$

If we can find a real x that satisfies $x < 1$, then we have the solution

$$t_B(A, \theta) = \cos^{-1} x, \tag{B7}$$

or else if there is no solution for x, then from equation (B2) we take $\sin t = 0$ which gives t = 0°, 180° depending on the quadrant.

[39] **Acknowledgments.** The Los Alamos Magnetospheric Plasma Analyzer (MPA) measurements were obtained from the CDAWeb data service at NASA Goddard Space Flight Center. We thank M. F. Thomsen for permission to use the MPA data. We also thank Shawn Young for reading the revised manuscript. The work of Maurice Tautz was done done under contract F19628-00-C-0089.

[40] Shadia Rifai Habbal thanks Jean-Francois Roussel and another referee for their assistance in evaluating this paper.

References

Bame, S. J., et al. (1993), Magnetospheric plasma analyzer for satellites with constrained resources, *Rev. Sci. Instrum.*, *64*(4), 1026–1033.

Besse, A., and A. Rubin (1980), A simple analysis of spacecraft charging involving blocked photoelectron currents, *J. Geophys. Res.*, *85*(A5), 2324–2328.

Feurenbacher, B., and B. Fitton (1972), Experimental investigation of photoemission from satellite surface materials, *J. Appl. Phys.*, *43*, 1563–1572.

Higgins, D. (1979), An analytic model of multi-dimensional spacecraft charging fields and potentials, *IEEE Trans. Nucl. Sci.*, *26*(6), 5162–5167.

Hinteregger, H. E., K. R. Damon, and L. A. Hall (1959), Analysis of photoelectrons from solar extreme ultraviolet, *J. Geophys. Res.*, *64*, 961–964.

Lai, S. T. (1994), An improved Langmuir probe formula for modeling satellite interactions with near-geostationary environment, *J. Geophy. Res.*, *99*(A1), 459–467.

Lai, S. T., H. A. Cohen, T. L. Aggson, and W. J. McNeil (1986), Charging of booms on a satellite rotating in sunlight, *J. Geophys. Res.*, *91*(A11), 12,137–12,141.

Mandell, M., I. Katz, G. Schnuelle, P. Steen, and J. Roche (1978), The decrease in effective photo-currents due to saddle points in electrostatic potentials near differentially charged spacecraft, *IEEE Trans. Nucl. Sci*, *26*(6), 1313–1317.

Olsen, R. C. (1980), Differential and active charging results from the ATS spacecraft, Ph.D. thesis, Univ. of Calif., San Diego, La Jolla, Calif.

Olsen, R. C., C. E. McElwain, and E. C. Whipple (1981), Observations of differential charging effects on ATS-6, *J. Geophys. Res.*, *86*(A8), 6809–6819.

Olsen, R. C., and E. C. Whipple (1988), An unusual charging event on ISEE 1, *J. Geophys. Res.*, *93*(A6), 5568–5578.

Powell, C. J. (1970), Analysis of optical and inelastic electronscattering data. III Reflectance data for beryllium, germanium, antimony, and bismuth, *J. Opt. Soc. Am.*, *60*(2), 214–220.

Samson, J. A. R. (1967), *Techniques of Ultraviolet Spectroscopy*, John Wiley, Hoboken, N. J.

Schwartz, M. (1972), *Principles of Electrodynamics*, McGraw-Hill, New York.

Stevens, J. R., and A. L. Vampola (Eds.) (1978), Description of the space test program P78-2 spacecraft and payloads, *Rep. SAMSO-TR-78-24.*, *ADA-06-1324*, Air Force Sys. Command, Los Angeles, Calif.

Tautz, M. (2003), Analytic models for sunlight charging of a rapidly spinning satellite, *AFGL-TR-2003-1557*, *ADA416912*, Air Force Res. Lab., Hanscom Air Force Base, Mass.

Thiebault, B., A. Hilgers, E. Sasot, H. Laakso, O. Escoubet, V. Genot, and J. Forest (2004), Potential barrier in the electrostatic sheath around a magnetospheric spacecraft, *J. Geophys. Res.*, *109*, A12207, doi:10.1029/2004JA010398.

Thomsen, M. F., E. Noveroske, J. E. Borovsky, and D. J. McComas (1999), Calculation of moments from measurements by the Los Alamos Magnetospheric plasma analyzer, *Rep. LA-13566-MS*, Los Alamos Natl. Lab., Los Alamos, N. M.

Whipple, E. C. (1981), Potentials of surfaces in space, *Rep. Progr. Phys.*, *44*, 1197–1250.

Wrenn, G. L., and W. L. Heikkila (1973), Photoelectrons emitted from ISIS spacecraft, in *Photons and Particle Interactions With Surfaces in Spaces*, edited by R. J. L. Grard, pp. 221–230, Springer, New York.

Zhao, H., R. Schmidt, C. P. Escoubet, K. Torkar, and W. Riedler (1996), Self-consistent determination of the electronic potential barrier due to the photoelectron sheath near a spacecraft, *J. Geophy. Res.*, *101*, 15,653–15,659.

S. T. Lai, Space Vehicles Directorate, Air Force Research Laboratory, Hanscom Air Force Base, MA 01731-3010, USA. (shu.lai@hanscom.af.mil)

M. Tautz, AER/Radex Inc., Lexington, MA 02421, USA.